Energy Reviews 1 (2022) 100007

Contents lists available at ScienceDirect

Energy Reviews

journal homepage: www.journals.elsevier.com/energy-reviews

Fluid injection-induced fault slip during unconventional energy development: A review

Wei Wu [a,*], Dazhao Lu [a], Derek Elsworth [b]

[a] School of Civil and Environmental Engineering, Nanyang Technological University, Singapore
[b] Departments of Energy and Mineral Engineering & Geosciences, Pennsylvania State University, USA

ARTICLE INFO

Keywords:
Fluid injection
Induced seismicity
Fault slip
Unconventional energy
Earthquake mitigation

ABSTRACT

An unusual increase in seismicity rate near the development and production sites of unconventional energy (e.g., natural gas and geothermal fluids) has been attributed to subsurface fluid injection. Damaging and hazardous earthquakes in many countries (e.g., China, South Korea, and the United States) have motivated tremendous effort to understand the complexity of fault slip behaviors in response to fluid pressurization. This study reviews key characteristics of injection-induced fault slip and highlights prediction and mitigation strategies relevant to unconventional energy projects. This capability relies on adequate understanding and characterization of first- and second-order friction and stability behaviors of faults as well as impacts of fluid pressurization and its role in triggering aseismic, seismic, and transitional slip behaviors. Suitable methods of investigation and characterization are noted together with typical examples together with scientific advances in our understanding towards forewarning and mitigation. Present challenges are addressed relating to the understanding of complex second-order friction behaviors and the location and characterization of blind faults. These needs are aided in the integration of multi-scale and multi-physical data obtained from laboratory, numerical, and field studies to offer crucial information for induced hazard preparedness and rapid run-up assessment. Finally, emerging technologies contributing to an improved understanding, such as data analytics and machine learning, are discussed in heralding the next frontier for injection-induced seismicity research.

1. Introduction

The quickening pace of the transition to clean and renewable energy relies heavily on subsurface fluid injection in the development of unconventional energy sources (e.g., natural gas as a transitional fuel and geothermal fluids). Injection operations desire to improve fracture connectivity and fluid circulation but in doing so also perturb the stress state on surrounding faults. In the recent two decades, an unusual increase in seismicity rate has occurred near unconventional energy projects and been attributed to fluid injection-induced fault reactivation. Earthquake moment magnitudes have been significant, such as the moment magnitude (M_w) 5.5 earthquake at Pohang, South Korea in 2017 due to stimulation of a deep geothermal reservoir [1], three $M_w \geq 4.7$ earthquakes in Sichuan, China in 2017–2019 during shale gas production [2], and twenty-four $M_w > 4.0$ earthquakes in Oklahoma, the United States in 2014 after fracking wastewater disposal [3]. These human-induced earthquakes have attracted considerable public attention and become an important topic of political and scientific discussion [4,5]. Several studies attempt to understand the mechanisms of injection-induced earthquakes and to mitigate the risks of seismic events [6,7]. For example, near-real-time seismic monitoring combined with a traffic light system has demonstrated success in controlling the moment magnitude of seismic events in geothermal reservoirs [8–10]. However, challenges remain as the latest evidence shows that both the transition from aseismic to seismic slip and the interaction between pressurized faults inside reservoirs and tectonic faults outside make fault slip behaviors unpredictable and uncontrollable [11]. Injection-induced aseismic slip may result in the remote occurrence of seismic events, which cannot be explained by poroelastic stress change and pore pressure diffusion [12]. Injection-induced fault interactions may result in dynamic triggering from main faults to secondary faults with local stress perturbations dominating over regional stress conditions [13]. Hence, understanding mechanisms and controls of injection-induced fault slip is critical in the forewarning and mitigation of anthropogenic earthquakes in unconventional energy projects.

Injection-induced fault slip can be classified into three modes: creep-and-slow slip, aseismic slip, and seismic slip, as based on peak slip

* Corresponding author.
E-mail address: wu.wei@ntu.edu.sg (W. Wu).

https://doi.org/10.1016/j.enrev.2022.100007
Received 5 September 2022; Received in revised form 27 September 2022; Accepted 27 September 2022

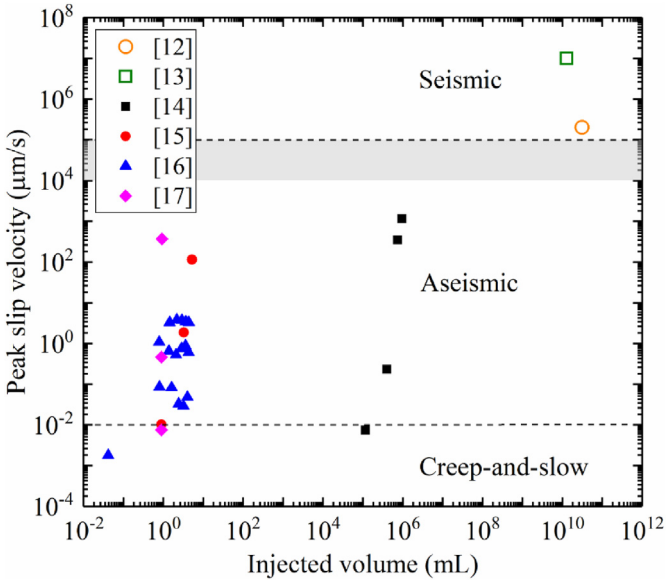

Fig. 1. Peak slip velocity as a function of injected volume and classification as creep-and-slow slip, aseismic slip, and seismic slip based on peak slip velocity. The grey area denotes region of aseismic-seismic transition.

velocity. The velocity boundaries separating these slip modes are not unified in the various laboratory and field studies [12–17]. Many laboratory experiments distinguish between aseismic and seismic slip based on whether acoustic emission signals are detected [18,19]. However, the peak velocity of so-called seismic slip is much lower than that of field-observed seismic slip, thus the seismic characterization of laboratory-scale artificial faults may not fully represent that of field-scale natural faults. Our understanding can thus be misled and confused by inconsistent descriptions of these slip modes. To assess the impacts of this terminological issue, we adopt 10^{-2} μm/s as the velocity boundary between creep-and-slow and aseismic slip and 10^{5} μm/s as the velocity boundary between aseismic and seismic slip [20]. As shown in Fig. 1, the peak slip velocities obtained from laboratory experiments mostly fall in the region of aseismic slip and are unlikely to reach the aseismic-seismic transition. The peak slip velocities measured in field experiments possibly transit the velocity boundary between aseismic and seismic slip but remain far below those from natural tectonic earthquakes. Therefore, a review on injection-induced fault slip is timely and necessary to summarize the current progress of injection-induced seismicity research and to ensure the efficient development of unconventional energy resources.

Numerous fundamental and applied investigations have significantly improved our understanding of injection-induced fault slip. However, significant knowledge gaps remain. These include the forewarning and mitigation of induced seismic events both within and beyond the duty-life and geographical extent of unconventional reservoirs, the utility of integration of multi-scale and multi-physical data obtained from laboratory, numerical, and field studies, as well as the impact of coupled thermo-hydro-mechanical-chemical processes in influencing the response of seismogenic faults. This review first summarizes the theoretical frameworks of fault friction and its applications to fluid injection-indued fault slip. The subsequent sections then focus on the investigation and characterization of injection-induced aseismic slip and potential transition to seismic slip. The discussion section finally addresses new strategies and interdisciplinary approaches that could accelerate the progress of injection-induced seismicity research.

2. Theories of fault friction

Early studies on the transition from static to dynamic friction date to the 1950s [21] and show that the friction coefficient varies as a function

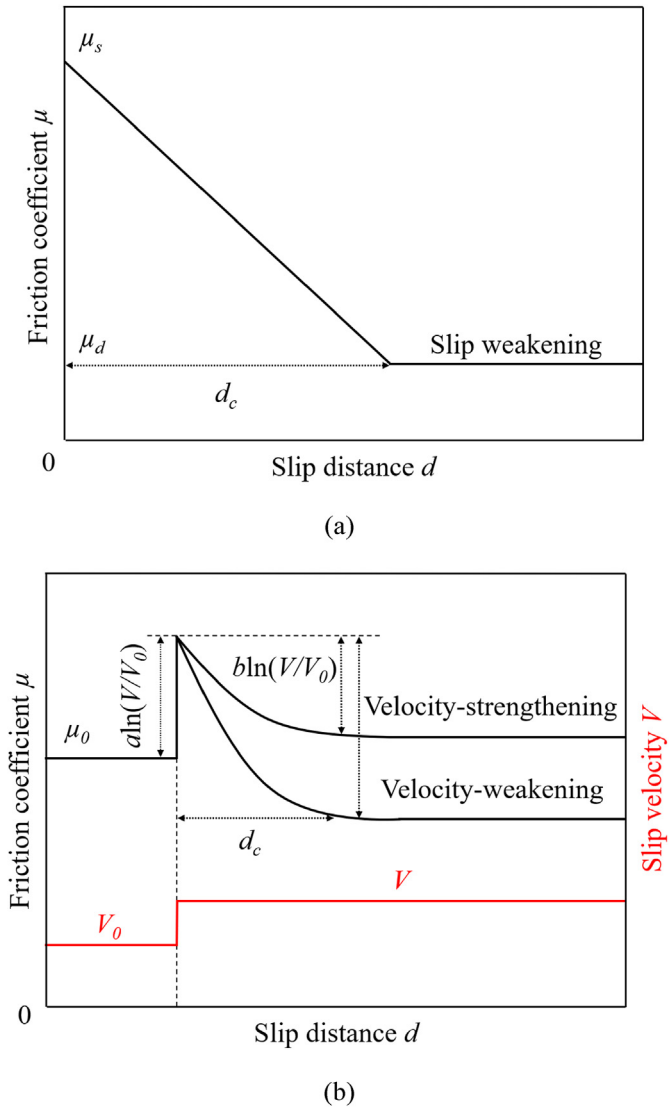

Fig. 2. Schematic diagrams of (a) slip-weakening friction and (b) rate-and-state friction.

of slip distance d and can be described by slip-weakening friction law [22,23] (Fig. 2a):

$$\mu(d) = \begin{cases} \mu_s - \dfrac{\mu_s - \mu_d}{d_c} d \ (d \le d_c) \\ \mu_d \ (d > d_c) \end{cases} \quad (1)$$

where μ_s and μ_d are the static and dynamic friction coefficients, respectively, and d_c is the characteristic slip distance.

Based on this slip-weakening friction law, the slip evolution of a pre-existing, fluid-pressurized fault is controlled by the fault stress criticality (the background shear stress τ_0 over the peak shear stress τ_p), the fluid injection condition (the fluid pressure perturbation Δp over the effective normal stress $\bar{\sigma}$), and the friction weakening ratio (the residual friction coefficient μ_r over the peak friction coefficient μ_p). Fig. 3 shows the ultimately stable regime and the unstable regime of the fault under the conditions of constant fluid overpressure and constant injection rate [24,25]. The friction weakening ratio determines the boundary between the ultimately stable regime and the unstable regime. For a constant fluid overpressure (Fig. 3a), the slip evolution is associated with the stress criticality and the fluid overpressure and can be classified into five regimes: (I) no slip (due to insufficient fluid overpressure), (II) slip arrest

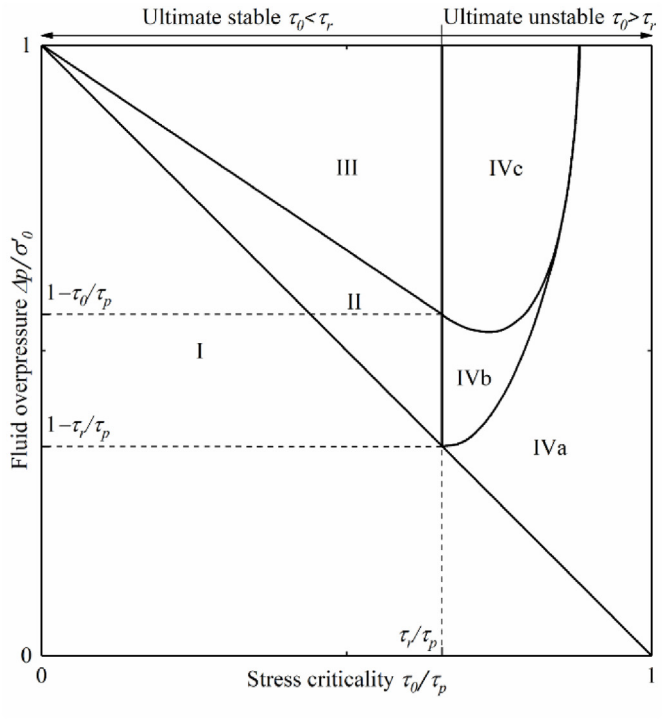

(a)

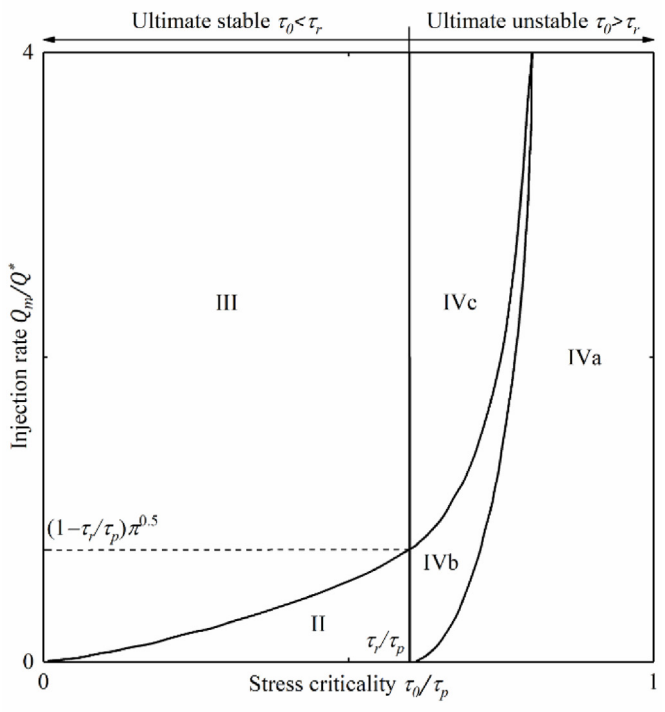

(b)

Fig. 3. Slip evolution on a fluid pressurized fault under (a) constant fluid overpressure (Reproduced with permission [24], Copyright 2012, John Wiley and Sons) and (b) constant injection rate (Reproduced with permission [25], Copyright 2022, Springer Nature).

(ultimately stable fault), (III) quasi-static slip (due to large fluid overpressure on ultimately stable fault), (IVa) unabated dynamic rupture (not affected by the residual frictional strength τ_r), (IVb) re-nucleation of unabated dynamic rupture, and (IVc) nucleation of dynamic slip (affected by τ_r and leading to unabated dynamic rupture). The slip evolution induced by a constant injection rate is related to the stress criticality and the normalized maximum injection rate (the maximum injection rate Q_m over the characteristic injection rate $Q^* = \frac{2\bar{\sigma}w_h k_f}{a_w \upsilon}$, where w_h is the hydraulic aperture, k_f is the fault permeability, a_w is the slipping patch length scale, and υ is the viscosity parameter) and can be divided into (II) slip arrest, (III) quasi-static slip, (IVa) unabated dynamic rupture, (IVb) re-nucleation of unabated dynamic rupture, and (IVc) nucleation of dynamic slip (Fig. 3b). Regime (I) is not shown here as fluid injection at a constant injection rate continually amplifies the fluid pressure and eventually induces the fault slip.

The time- and velocity-dependence of rock friction has been noted since the 1970s as derived from laboratory observations [26,27]. Rate-and-state friction laws have been developed as [28,29] (Fig. 2b):

$$\mu = \mu_0 + a\ln\left(\frac{V}{V_0}\right) + b\ln\left(\frac{V_0\theta}{d_c}\right) \tag{2}$$

where μ and μ_0 are the friction coefficients at the slip velocities of V and V_0, respectively, a and b are the coefficients representing rate and state dependencies, respectively, and θ is a state variable indexing progress from initial to final state. The velocity dependence is indexed through the sign of $(b-a)$. When $(b-a)>0$, the fault is velocity-weakening and potentially unstable. When $(b-a)<0$, the fault is velocity-strengthening and intrinsically stable. Thus, the transition between unstable and stable slip occurs at $(b-a) \sim 0$ when the fault is velocity-neutral. The rate-and-state friction laws can be used as a theoretical basis to simulate a wide range of slip modes, including creep-and-slow slip, aseismic slip, and seismic slip [30,31].

Velocity-weakening response $(b-a)>0$ is a necessary but insufficient condition for seismic slip. Fault instability is conditioned by the stiffness ratio $K = k/k_c$, where k is the stiffness of surrounding rock, and k_c is the rheologic stiffness of the fault [32]. $K \sim 1$ represents transitional behavior between unstable $K<1$ and stable $K>1$ modes. Unstable response may be driven by increasing the rheologic stiffness of the material comprising the fault or decreasing the geometric stiffness G/l of the fault, typically by increasing the patch size l relative to the near-invariant shear modulus of the geologic host G.

The additive formulation of the rate-and-state friction laws is ill-posed for vanishing slip velocity and valid only for a narrow range of slip velocities. The multiplicative form is thus derived based on the assumption that the slip velocity is controlled by the real area of asperity contacts [20,33]:

$$\mu = \mu_0\left(\frac{V}{V_0}\right)^{\frac{a}{\mu_0}}\left(\frac{V_0\theta}{d_c}\right)^{\frac{b}{\mu_0}} \tag{3}$$

The multiplicative form has advantages of explaining the correlation between the gouge thickness and the characteristic slip distance, the correlation between the static friction coefficient and the rate and state dependencies and the temperature dependence of frictional resistance.

A dimensional analysis of rate-and-state friction reveals that fault dynamics is dictated by three non-dimensional parameters: the static friction coefficient μ_0, the inverse of the stiffness ratio R_u, and the frictional property ratio R_b [33,34]:

$$R_u = \frac{(b-a)\bar{\sigma}}{kd_c} = \frac{k_c}{k} \tag{4}$$

$$R_b = \frac{(b-a)}{b} \tag{5}$$

where $\bar{\sigma}$ represents the effective normal stress, R_u describes the stability and rupture styles and is related to the characteristic nucleation size, and R_b controls the dynamic and static stress drops and classifies response as

either velocity-strengthening ($R_b < 1$), velocity-neutral ($R_b \sim 1$), or velocity-weakening ($0 < R_b < 1$).

Compared to a rate-and-state friction law with a variable fiction coefficient, a coupled shear rupture model assumes a constant friction coefficient and emphasizes the competition between advance of the aseismic slip front relative to the fluid diffusion front [35]. For a one-dimensional shear crack extending along a planar fault, if the stress intensity factor for the edge crack is zero, the fault stress parameter $T = \left(1 - \frac{\tau}{\mu\bar{\sigma}}\right) \frac{\bar{\sigma}}{\Delta p}$ can be written as a function of an aseismic slip front amplification factor λ:

$$\left(1 - \frac{\tau}{\mu\bar{\sigma}}\right) \frac{\bar{\sigma}}{\Delta p} = \frac{1}{\pi} \int_{-1}^{1} \frac{erfc(|\lambda\eta|)}{\sqrt{1-\eta^2}} d\eta \tag{6}$$

where τ is the shear stress and η is the ratio of the along-fault distance from the injection point to the half-length of fault rupture and ranges from -1 to 1. λ is defined as the ratio of the half length of fault rupture $a(t)$ to the half length of fluid diffusion $\sqrt{\alpha t}$, where α is the hydraulic diffusivity, and t is the elapsed time. $\lambda > 1$ indicates that the aseismic slip front outpaces the fluid diffusion front and extends beyond the pressurized area, while $\lambda < 1$ means that the aseismic slip front falls behind the fluid diffusion front and is confined within the pressurized area. $\lambda = 1$ corresponds the transition between the aseismic slip front and the fluid diffusion front.

The concept of λ can be generalized to describe the competition between the progress of the aseismic slip front relative to the fluid diffusion front for a two-dimensional shear crack [36]. The aspect ratio of fault rupture depends on the fault stress parameter T and the Poisson's ratio υ. For $\upsilon = 0$, the rupture front is circular and λ is defined as given in Eq. (6). For $\upsilon \neq 0$, the rupture front is elliptical and $\lambda = \sqrt{\lambda_a \lambda_b}$, where λ_a and λ_b are the aseismic slip front amplification factors for in-plane slip and out-of-plane slip, respectively.

3. Injection-induced aseismic slip

Early observations of injection-induced aseismic slip reported in the late 20th century show that seismic slip triggered in less overpressured regions may be induced by stress transfer as a result of aseismic deformation in more highly pressured regions. This observation may explain the time delay between the start of fluid injection and the onset of induced seismicity [37] and the lack of typical foreshocks and aftershocks triggered in conjunction with a mainshock [38]. Aseismic slip on a fault zone identified during a series of hydraulic tests at the Le Mayet de Montagne granite test site in central France was found to contribute to the variation of the regional stress field [39]. Aseismic slip was also observed during water injection tests at the Soultz-sous-Forêts hot dry rock test site in northeastern France and attributed as a cause for an inaccurate evaluation of stimulation efficiency based solely on the frequency analysis of induced seismic signals [40]. These observations inspired the investigation of the role of aseismic slip in the occurrence of injection-induced seismicity during the development of unconventional energy.

Due to the fast growth of unconventional energy projects in the early 21st century, injection-induced aseismic slip was frequently detected during hydraulic fracturing [41], gas storage [42], and wastewater disposal [43] operations. A stable, swarm-like foreshock sequence is a characteristic signature of aseismic response, ultimately triggering the mainshock in a nearby region [44]. As the jettisoned aseismic energy is below the detection limit of the seismic monitoring system, aseismic slip can be measured by creepmeters [45], Interferometric Synthetic Aperture Radar (InSAR) [46], Global Positioning Systems (GPS) [47], borehole strainmeters [48], and Light Detection And Ranging (LiDAR) systems [49]. These monitoring methods with their attendant spatial and temporal measurement resolutions and survey scales, together with typical applications, are summarized in Table 1. In practice, multiple monitoring methods are jointly applied to confirm the detection of aseismic slip – as they span a range of length- and time-scales and resolutions. For example, InSAR and leveling measurements, together with waveform inversions and field observations, revealed that aseismic slip occurred on a shallow normal fault beneath the North Brawley geothermal field in southern California, followed by the 2012 earthquake sequence [50]. Hence, reliable detection and deliberative analysis of aseismic slip can improve the forewarning of major earthquakes.

Table 1
Aseismic slip monitoring methods and their spatial and temporal resolutions of measurement, survey scale and typical applications.

Method	Spatial resolution	Temporal resolution	Survey scale	Typical application
Creepmeters [45]	micrometer	minute	m	Local recording of preseismic, coseismic, and postseismic slip rates
InSAR [46]	millimeter	day	km	Spatial and temporal variation of surface deformation
GPS [47]	centimeter	second	km	Continuous observation of aseismic deformation transient
Borehole strainmeter [48]	nanostrain	millisecond	m	High-sensitivity measurement for periods of seconds to months
LiDAR [49]	millimeter	second	m	3D monitoring of surface creep along pre-existing faults

Deciphering mechanisms of injection-induced aseismic slip from complex and noisy observations can be challenging as the complexity of geologic environments usually blurs the aseismic features. Well controlled and closely monitored field experiments are thus useful to understand slip processes and constrain key controls. A water injection experiment at the Laboratoire Souterrain à Bas Bruit (LSBB) in southeast France observed aseismic slip on a natural fault (Fig. 4a) as a result of forced reactivation. Tight control and constraint on injection rate, direct measurement of resulting slip displacement and seismic moment together with subsequent evaluation of the evolution of friction coefficient and fault permeability reveal that the resulting aseismic slip is a direct consequence of the water injection with the fault exhibiting intrinsically velocity-strengthening behavior [14]. Numerous studies follow this field experiment to further investigate the mechanisms of injection-induced aseismic slip. A three-dimensional Distinct Element Code (3DEC) model reveals that fluid injection first promotes slip acceleration and then fault dilation on pressurized patches near the injection point before inducing seismic slip on the non-pressurized, remote patches due to poroelastic stress transfer [51]. An adjunct to this 3DEC model illustrates that the aseismic slip front outpaces the fluid diffusion front [52], and a 3D inherently discrete rupture model also exhibits the correlation between the migration rates of the aseismic slip and seismicity fronts [53]. The competition among the aseismic slip front, the fluid diffusion front, and the shear stress transfer front essentially controls the occurrence of induced seismic events [17] (Fig. 4b). A 2D boundary integral model quantifies the fault friction and indicates that mitigation of subsequent seismic slip may be achieved by avoiding fluid injection into low-friction patches and by reducing injection pressure during slip acceleration [54].

Although our understanding of injection-induced aseismic slip remains limited, conditions favorable for the occurrence of aseismic slip have been explored through various analytical and experimental studies. Many analytical models are built based on rate-and-state friction and principally focus on repeating sequences containing both aseismic and seismic events. For example, a poroelastic model of earthquake

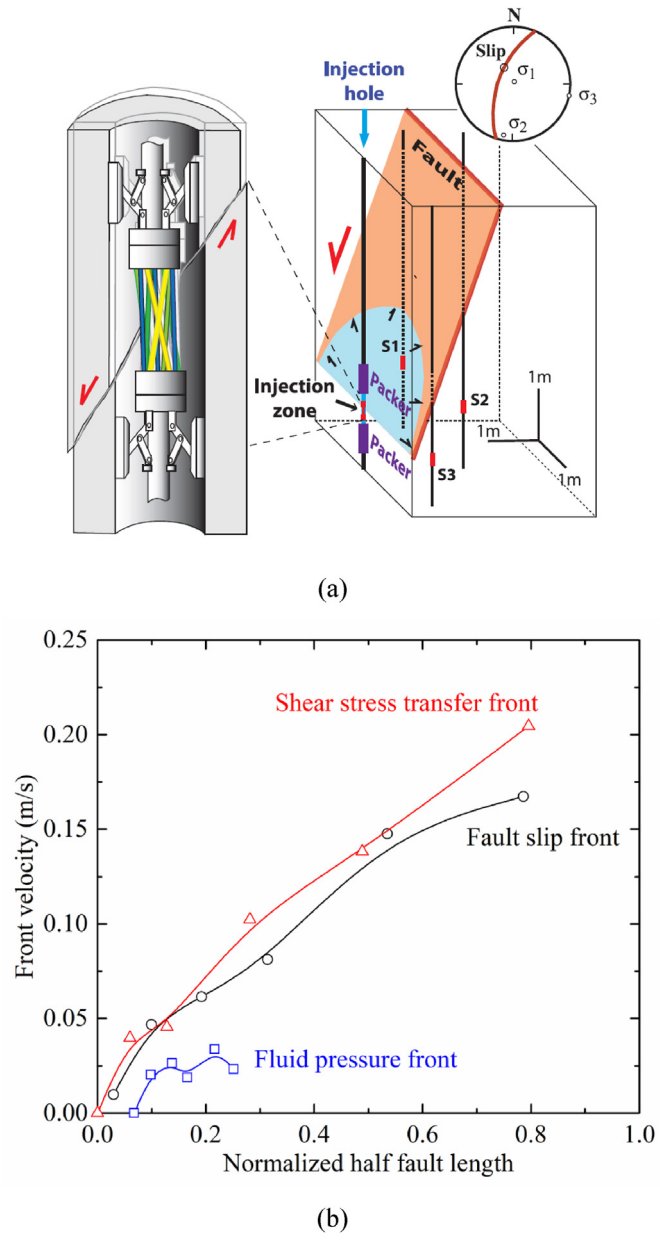

Fig. 4. Water injection experiment at LSBB, (a) experimental apparatus and deployment with displacement sensor measuring shear reactivation displacements on fault (left) and injection borehole piercing the fault (right) (Reproduced with permission [14], Copyright 2015, American Association for the Advancement of Science) and (b) propagation velocities of aseismic slip front, fluid diffusion front, and shear stress transfer front along the fault (Reproduced with permission [17], Copyright 2022, Springer Nature).

nucleation demonstrates that a gradual step-up injection protocol likely promotes aseismic slip [55] while an anti-plane fault model reveals that fault dilatancy may also hinder the propagation of aseismic slip [56]. Laboratory experiments replicate aseismic slip on pre-existing faults and show that aseismic slip is controlled by fault surface roughness and host rock minerology. Aseismic slip is readily observed on rougher faults in granite [18] and on phyllosilicate-rich faults in shale [57]. Aseismic slip can also be influenced by coupled thermo-hydro-mechanical-chemical process [10], particularly the coupling among fluid flow, aseismic slip, as well as the evolution of fault permeability under changes in the pressure distribution [58]. This improved understanding of aseismic slip has contributed to reveal the seismogenic state of pressurized faults [59] and inform methods to modulate the occurrence of induced seismic events [60]. Additionally, thermal destressing, resulting from aseismic slip at low normal effective stresses due to thermal contraction, can ameliorate stress concentrations and potentially impede fault rupture [61].

4. Injection-induced slip transition

Multiple lines of evidence indicate that the complexity of natural and induced earthquakes is associated with the transition between seismic and aseismic slip behaviors which typically depends on fault characteristics (e.g., gouge compaction and elastic property [62]) and changing environmental conditions (e.g., slip velocity and stress condition [63]). A typical example of slip transition in nature is the period-doubling cycles of slow slip on the Parkfield segment of the San Andreas Fault in California. This is characterized by the regular oscillation of recurrence intervals between about 3 and 6 days and interrupted by the M_w 6.0 Parkfield earthquake in 2004 [64]. The recurrence intervals are recovered after two years due to a decrease in effective pore pressure [65]. Stepped-unloading friction experiments on granite faults using a direct-shear setup under a decreasing normal stress and a constant slip velocity (Fig. 5) show that a change in normal stress promotes the occurrence of period-doubling cycles and additionally incorporates their complex transitional behaviors (e.g., period-multiplying cycles and deterministic chaos) between stick-slip and stable sliding [66]. The laboratory analysis, based on the multiplicative form of the rate-and-state friction laws, reveals that transitional behaviors are sensitive indicators of fault stability and are controlled by the stiffness ratio ($K \sim 1$) and the frictional property ratio ($R_b \sim 1$) [34].

Although this slip transition has been rarely reported for unconventional energy projects, the evolution of injection-induced seismic events can be explained by the transitional behaviors. At the Soultz-sous-Forêts geothermal demonstration site in France, after the chemical stimulation, the number of induced seismic events near the injection well reduced during the post-acid water injection compared to that during the pre-acid water injection [67]. This is attributed to the slip transition from seismic to aseismic caused by the dissolution of rock-forming minerals due to the acid treatment [68]. Meanwhile, induced seismic events occurred in an expanded region during the post-acid water injection as the aseismic slip projected a shear stress imbalance along more distal faults, resulting in induced seismicity far beyond the injection well [69]. This slip transition can be explained through the aseismic slip front amplification factor. The concurrent variations of shear stress and fluid pressure due to fluid injection can be expressed as the ratio of the shear stress variation $\Delta\tau$ to the fluid pressure variation Δp by modifying Eq. (6) as:

$$\frac{\Delta\tau}{\Delta p} = \frac{\mu}{\pi}\int_{-1}^{1}\frac{erfc(|\lambda\eta|)}{\sqrt{1-\eta^2}}d\eta \tag{7}$$

Here the slip transition from aseismic to seismic occurs when $\lambda \sim 1$ based on the assumption of a constant friction coefficient. For an amplified friction coefficient, λ approaches 1 with a smaller reduction of the ratio $\Delta\tau/\Delta p$. As shown in Fig. 6, fluid is injected into a critically stressed, chemically treated fault in a triaxial cell. The treated fault with rough surfaces exhibits a deviation of the ratio $\Delta\tau/\Delta p$ from the analytical curve according to Eq. (7), resulting in an early occurrence of seismic events. A change in friction coefficient can also be considered with varying λ. Thus, shear-induced fault dilation may cause a smaller reduction in the ratio $\Delta\tau/\Delta p$ and further promote λ to unity [69] (Fig. 6).

The above natural and industrial cases highlight that the theories of fault friction are universally applicable to assess the transition between the aseismic and seismic slip behaviors. The mechanisms of slip transition upon fluid injection are commonly investigated using laboratory experiments, and many studies reveal that the slip transition is associated with fault properties and injection strategies [69,70]. In Grissal granite, plagioclase and calcite react readily with acid solution, and quartz and

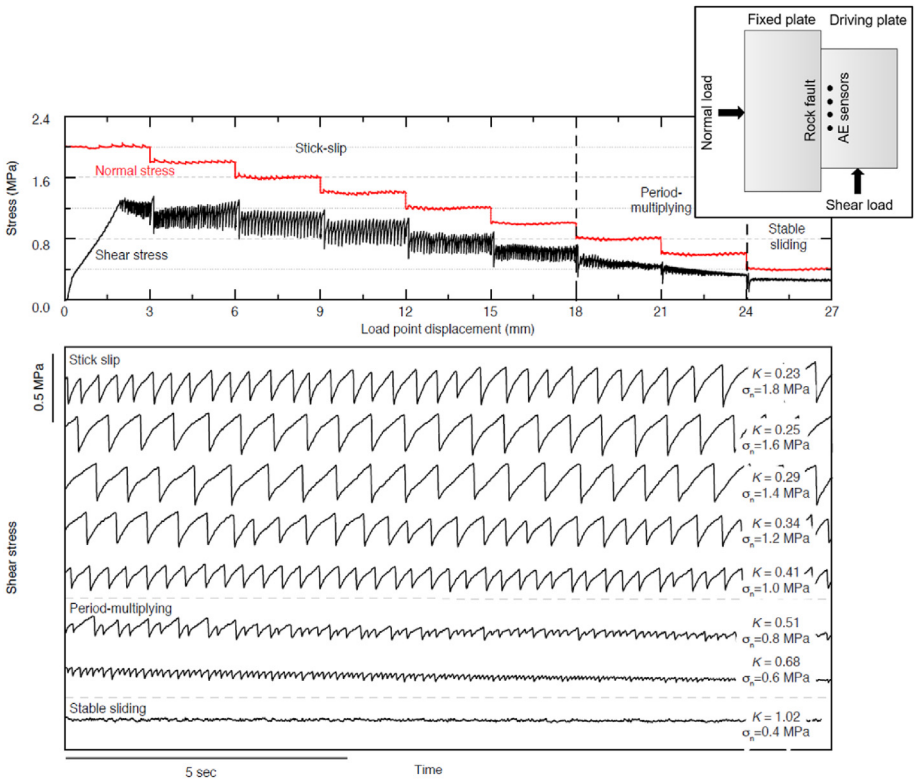

Fig. 5. Fault slip behaviors obtained from stepped-unloading friction experiments on granite faults (inset), including stick slip, period-multiplying, and stable sliding behaviors (Reproduced with permission [66], Copyright 2021, John Wiley and Sons).

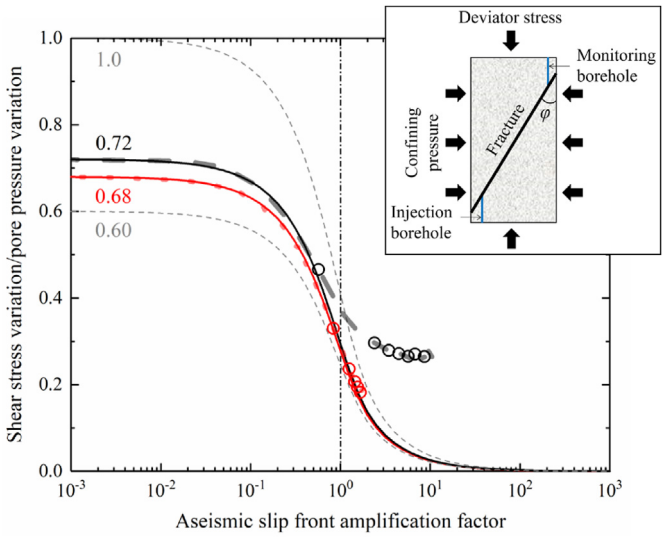

Fig. 6. Ratio of shear stress variation to fluid pressure variation as a function of aseismic slip front amplification factor (Reproduced with permission [69], Copyright 2022, Elsevier). The solid and dashed lines denote the analytical results based on Eq. (7) and the experimental results obtained from fluid injection experiments (inset), respectively. The open circles indicate individual seismic events.

mica are less reactive [68]. Hence, the tectosilicate (quartz and plagioclase) and carbonate (calcite) contents decrease, and the relative phyllosilicate (mica) content increases, resulting in a decrease in the $(b-a)$ value [71]. Laboratory faults in Green River shale and Poorman schist show that the slip transition is related to fault permeability evolution as well as frictional healing and sealing [72]. Fluid injection into fault gouges of marble and limestone cause slip evolution from velocity-strengthening to velocity-neutral/weakening with a decrease in the $(b-a)$ value [73], as fluid pressurization results in dilation of the fault and the acceleration of creep [74]. The slip transition is also controlled by hydraulic and thermal conditions. The oscillation of fluid pressure leads to a variation in slip velocity and a change in critical stiffness, again promoting slip transition [75]. For faults in Westerly granite, strain hardening and softening influence the velocity-weakening behavior below and above 350 °C, respectively [76].

5. Injection-induced seismic slip

Seismic triggering by fluid injection has been recognized as a causal mechanism for decades and quantified since instrumental observations have been available. For example, at least three mainshocks with body-wave magnitudes ranging from 4.4 to 5.5 were caused by fluid waste injection in the German Potash mining region in 1989 [77]. Injection-induced seismic slip commonly occurs with a slip velocity of $>10^5$ μm/s (Fig. 1) – a slip velocity difficult to achieve in laboratory and field experiments. Although rotary friction experiments can achieve high slip velocities [78] but are yet to be used in the study of injection-induced seismicity. Seismic slip accompanied by brittle rock failure and abrupt energy release is frequently recorded in unconventional energy projects and known as induced earthquakes. Hence, several numerical models have been developed to investigate mechanisms of full-scale seismic slip, such as CFRAC based on the displacement discontinuity boundary element code [79] and RSQSim based on the boundary element code [80]. Typical numerical codes, their applications, and implications for the seismic events they are analyzing are summarized in Table 2. These numerical studies are based on commonly accepted constitutive models (e.g., slip-weakening friction and rate-and-state friction) and demonstrate many significant characteristics of seismic slip, including fault growth and permeability evolution [81], dynamic rupture along impermeable faults [82], changes in fault poroelastic and thermal stresses [83],

and fluid flow diffusing in natural fracture networks and connecting with critically stressed faults [84].

One notable case of injection-induced seismic slip is the M_w 5.5 Pohang earthquake. This event occurred on November 15, 2017 [85,86], ~2 months after the completion of 5 hydraulic stimulation experiments (Fig. 7a). Fluid was injected through two injection wells (PX-1 and PX-2) drilled into the granitic basement at measured depths of 4362 and 4348 m, respectively. Careful examination of the geologic and stress conditions, seismic data and injection rates confirmed that the Pohang earthquake was triggered by the stimulation of well PX-2 [1]. Numerous studies have explored controls on the occurrence of the Pohang earthquake. The injection well (PX-2) is directly connected to a previously unmapped fault and fluid overpressurization occurred in the footwall of this fault [87]. The Coulomb static stress transfer associated with fluid overpressurization from the stimulated area (Fig. 7b) is one of the key mechanisms for the earthquake occurring remotely on the low-permeability fault [88]. Dynamic triggering from the main fault to the secondary fault via a jumping rupture could also explain the occurrence of this earthquake [13]. Many alternative methods have been tested analytically and numerically to predict the event and to define conditions *a posteriori* to mitigate the induced earthquake – including proper configuration of well operations [89] and real-time monitoring of hypothetical maximum seismic moment [90].

A variety of analytical models have been proposed and validated against observations to predict the maximum moment magnitude of injection-induced earthquakes. Many of these models scale moment magnitude to the volume of injected fluid via additional physical parameters representing reservoir characteristics, including shear modulus of the reservoir, frictional characteristics of the fault, seismogenic index, and stress criticality coefficient (Table 3). Statistical models [91] use a seismogenic index as the link between the maximum seismic moment and the injected volume and show that the number of induced earthquakes increases with an increase in injected volume and that magnitudes scale with injected volume to the power 3/2. For fluid injection into a fully saturated rock mass containing a fault favorably oriented for slip, the maximum seismic moment can be determined as the product of the injected volume, bulk modulus, and friction coefficient for the reservoir (approximated as the product of volume and shear modulus) [92] – the so-called McGarr model. This analysis requires that the rupture is contained within the fluid pressurized volume and that the seismic cycle is at mid loading. Relaxing these requirements for a pre-existing shear stress applied to the fault results in an increase in moment magnitude with injected volume that scales with a prefactor equal to the seismic stress ratio [93]. Such considerations of pre-stress enable, for

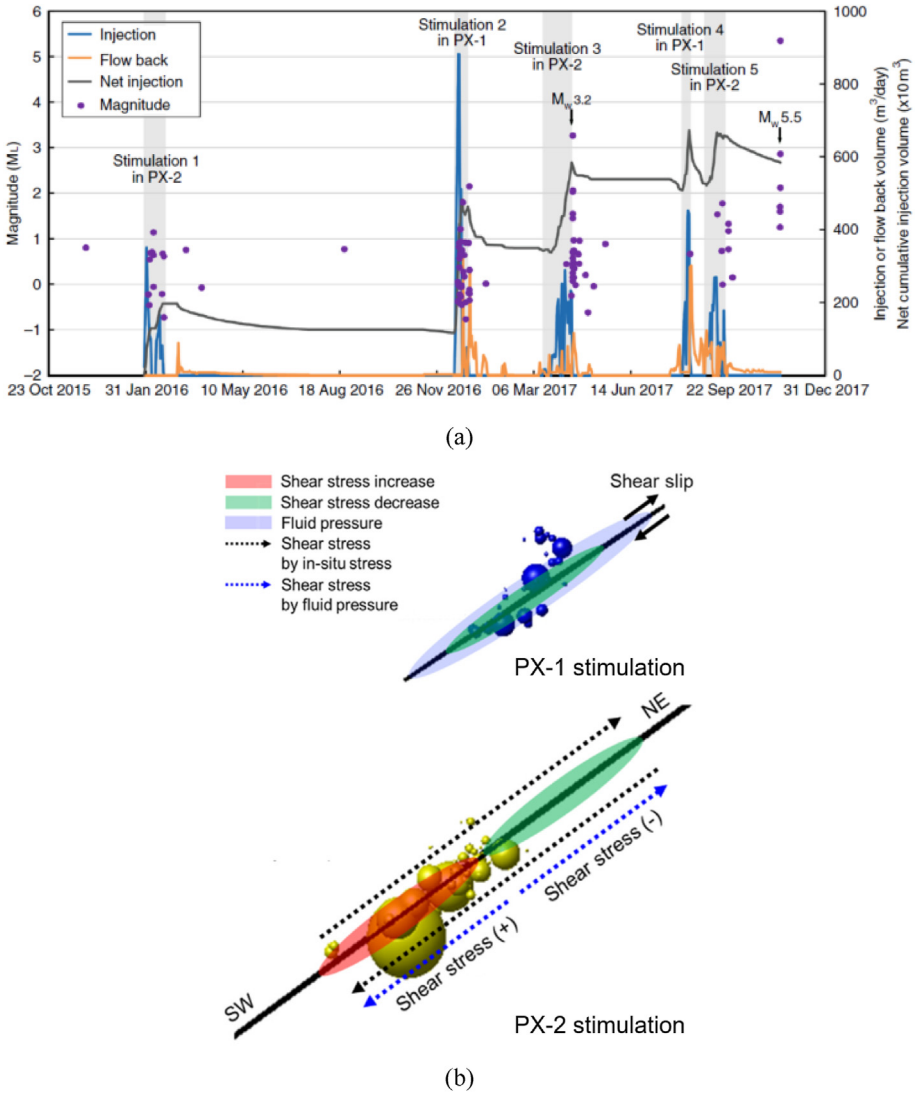

Fig. 7. Pohang EGS stimulation and induced earthquakes, (a) timeline of 5 hydraulic stimulations and injection-induced seismic events (Reproduced with permission [85], Copyright 2020, Springer Nature), and (b) injection-induced stress evolution near injection wells PX-1 and PX-2 (Reproduced with permission [88], Copyright 2022, Elsevier).

Table 2
Numerical codes used to understand injection-induced seismic slip.

Numerical code	Engineering background	Injected volume (m^3)/flow rate (L/s)	Triggering mechanism	Observed/ simulated magnitude (M_w)
Finite element code (SeisSol) [13]	Seismic faulting due to hydraulic stimulation at Pohang geothermal field, South Korea	12,798/47	Complex fault interaction and local stress perturbation due to fluid overpressure	5.5/5.63
Finite element code (COMSOL) [85]	Seismic faulting due to hydraulic stimulation at Pohang geothermal field, South Korea	12,798/47	Injection-induced slip of critically stressed faults and earthquake interaction due to static stress transfer	5.5/5.5
Finite difference code (FLAC3D) [81]	Hydraulic stimulation at Soultz-sous-Forêts geothermal field, France	37,300/20	Growth of fault zone with large directional permeability	2.9/3.0
Finite difference code (TOUGH-FLAC) [82]	Hydraulic fracturing at Marcellus shale play, United States	64,800/0.1	Slip and rupture of nearly impermeable fault due to hydraulic fracturing	2.8/1.7
Finite difference code (TOUGH-FLAC) [83]	Seismic and aseismic faulting at Brawley geothermal field, United States	2,000,000/ 154-656	Poroelastic and thermal stress changes induced by geothermal operations	5.4/5.4
Displacement discontinuity boundary element code (CFRAC) [79]	Wastewater disposal in Oklahoma, United States	267,840/ 10	Fault rupture inside and outside the pressurized region depending on fluid pressure perturbation	5.6/4.0
Boundary element code (RSQSim) [80]	Wastewater disposal and deep well brine injection in Colorado, United States	5,003,400/ 10	Changes of effective stress on the faults due to fluid injection	4.4/5.0
Distinct element code (3DEC) [84]	Hydraulic fracturing in Montney Formation, Canada	18-1800/ 10–1000	Influences of natural fracture network on fluid flow diffusion and connectivity with critically stressed fault	4.6/3.9

example, the excess moment magnitude recorded for the 2017 Pohang event to be reconciled with injection volume [93]. Prediction accuracy is heavily dependent on the estimation of input parameters (e.g., seismogenic index and reservoir parameter). In the prior models, the fault size and the normal stiffness are not explicitly considered, which have been shown to influence the maximum seismic moment [94,95]. Hence, a laboratory-based model additionally considers the fault radius, the stress criticality coefficient, and the fault normal stiffness to predict the maximum seismic moment [96]. The critical stress and the injected volume are defined as key parameters for predicting the maximum

Table 3
Analytical models for the prediction of maximum seismic moment $M_0(max)$ based on injected volume ΔV. G is the shear modulus of the reservoir rock, Σ is the seismogenic index, γ is a reservoir parameter, R is the fault radius, α is the stress criticality coefficient, k_n is the fault normal stiffness, and c is the fraction of the stress drop taken up before injection.

Model	Formula
van der Elst et al. [91]	$M_0(max) = 10^{\frac{3}{2}(\Sigma+6.07)}\Delta V^{\frac{3}{2}}$
McGarr [92]	$M_0(max) = G\Delta V$
Li et al. [93]	$M_0(max) = \frac{c}{1-c}G\Delta V$
Ji et al. [96]	$M_0(max) = \frac{8\mu R k_n}{7\pi\alpha}\Delta V$
Galis et al. [97]	$M_0(max) = \gamma\Delta V^{\frac{3}{2}}$

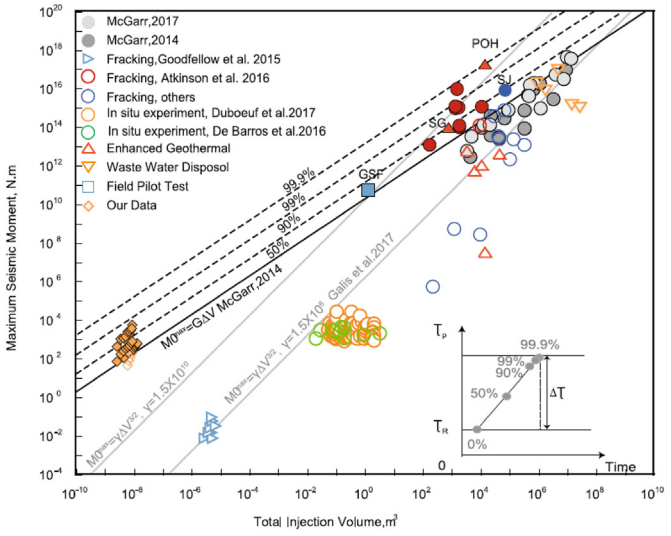

Fig. 8. Maximum seismic moment as a function of total injection volume for laboratory and field data against analytical predictions ([92,93,97]) (Reproduced with permission [93], Copyright 2021, Springer Nature).

seismic moment (Fig. 8), and a scaling factor $s = \mu\frac{k}{k_c}$ can be used to address the differences in geometries and constraints between laboratory and natural faults [93]. All these prior models contain the extent of fault rupture to within the pressurized volume and do not accommodate runaway ruptures. Models accommodating runaway rupture [97] scale moment magnitude as proportional to the injected volume, to the power 3/2 and conditioned by shear modulus, dynamic stress drop and pre-stress. These various relations for both constrained [92,93,96] and unconstrained [97] ruptures give similar predictive results and are equivocal, based on existing constraints and the historic earthquake record.

6. Discussion

The recent growth in scientific interest in injection-indued fault slip has resulted in improvements in our understanding and managing of fault reactivation and rupture propagation. New strategies in fluid injection, seismic monitoring, and decision making have been developed to ensure the safe and efficient development of unconventional energy resources. During fluid injection into a 6.1 km deep geothermal well near Helsinki, Finland from June to July 2018, near-real-time information on induced earthquakes (e.g., earthquake rate, location, and magnitude) was used to define the injection schedule. Operational feedbacks from a traffic light system (e.g., amber threshold for modification in injection rate, red threshold for terminating injection) suggest changes in injection rate and well-head pressure are able to achieve successful control of induced

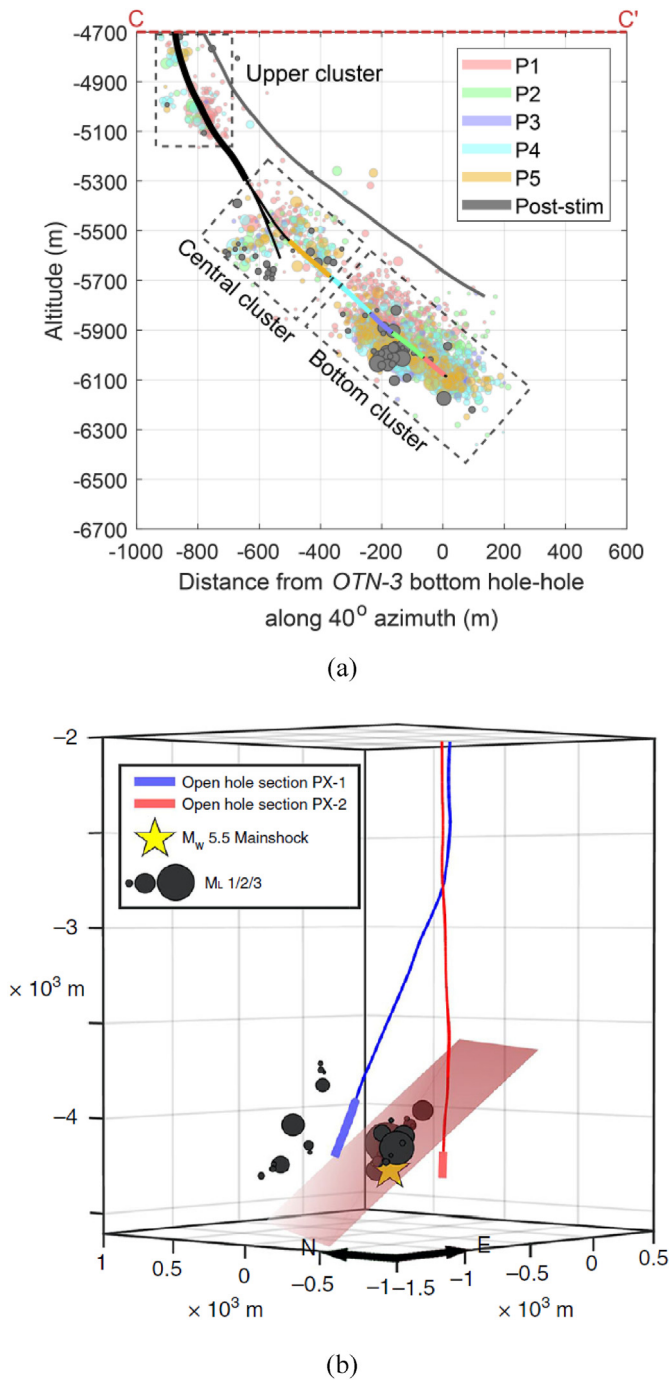

Fig. 9. Distributions of injection-induced seismic events adjacent to injection wells at (a) Helsinki, Finland (Reproduced under the Creative Commons Attribution 4.0 License [98], Copyright 2021, Copernicus Publications) and (b) Pohang, Korea (Reproduced with permission [85], Copyright 2020, Springer Nature).

earthquakes with M_w<2.0 [98]. Likewise, the cyclic soft stimulation at the Pohang enhanced geothermal systems site was designed to limit the induced seismic events to M_w<2.0, again using seismic real-time monitoring with a traffic light system during the 7–14 August 2017 fluid injection [8]. This cyclic soft stimulation was performed through well PX-1 while the Pohang earthquake was directly linked to fluid injection in well PX-2 [87]. Fig. 9 compares the distributions of induced seismic events for the Helsinki and Pohang cases and highlights different mechanisms involved in these seismic events. The seismic events at the Helsinki site are induced along the injection well during the 5 stimulation phases (Fig. 9a). No clear alignment of seismic events extends beyond the injection well, indicating that seismogenic faults may not exist or are not activated by fluid injection. For the Pohang site, the concentration of seismic events between two injection wells reveals that the induced earthquake was initiated on a critically stressed fault and triggered by fluid injection (Fig. 9b), resulting in a release of tectonic strain energy [99]. This demonstrates that our current strategies can predict and mitigate injection-induced seismicity close to the injection well or even within unconventional reservoirs. However, our characterization and understanding of the response of seismogenic faults, especially those remote from the injection site, remains inadequate. Managing fault slip behaviors upon fluid injection has become one of the major challenges to the development of unconventional energy resources.

Although a staggering trove of seismic data has been collected from various field and laboratory experiments, key mechanisms of injection-induced fault slip remain poorly constrained – the key to an improved understanding relies heavily on how to analyze and interpret the data. Creative analysis of such seismic data beyond traditional theories and approaches may result in improvements in prediction and mitigation of induced seismic events. Recent developments in data analytics and machine learning opens a new means to characterize seismic data and to further understand earthquake mechanisms. An unsupervised machine learning model is used to study the aftershock sequence of the Pohang earthquake and to improve the assessment of the induced geohazard [100]. Similarity, a correlation between seismic events induced by hydraulic fracturing operations in the Montney Formation, Canada and the estimated seismogenic reactivation potential is established based on a supervised machine learning model. This has proved useful to determine areas where hydraulic fracturing operations potentially induce hazardous seismic events [101]. Machine learning algorithms are also applied to reveal important predictors for the forewarning of induced earthquakes (e.g., proximity to basement, in-situ stress magnitude, natural seismicity rate, etc.) [102], primary (e.g., injected volume and shut-in pressure) and secondary (e.g., formation thickness and breakdown pressure) influences on the distribution of injection-induced seismic events [103], and changes in acoustic properties and faulting processes associated with changes in thermo-mechanical features [104]. The main challenges of these studies are the paucity of data and can be addressed via transfer learning [105]. As shown in Fig. 10, machine learning models trained on numerical simulations and fine-tuned with limited laboratory or field data are capable of replicating response. Data-driven discovery has shown its potential for solving long-standing problems in solid earth geosciences [106], and further improvements of our understanding of injection-indued fault slip are expected with the aid of multidisciplinary approaches.

7. Conclusions

Understanding injection-induced fault slip is a key emerging topic that has attracted extensive attention as unconventional energy resources become significant for a clean, affordable and reliable energy future. This review provides a critical and comprehensive overview of injection-induced fault slip and reveals fundamental shortcomings in our present understanding of fault slip behaviors. Well constrained laboratory fault reactivation experiments suitable for systematically examining fault characteristics cannot generally approach the peak velocity and shear offsets of field-scale seismic slip. However, the investigation and characterization of aseismic, seismic, and transitional slip behaviors indicate that reliable detection and thoughtful interpretation of the collected data from natural faults is crucial for geohazard assessment, and that, the slip transition is a promising indicator for fault instability. The study also demonstrates that better understanding of fluid pressure diffusion, aseismic slip propagation, and static stress transfer on low-permeability, seismogenic faults can motivate more robust strategies for the management of geohazard risk. Further effort is required to predict and mitigate damaging earthquakes during unconventional energy development with

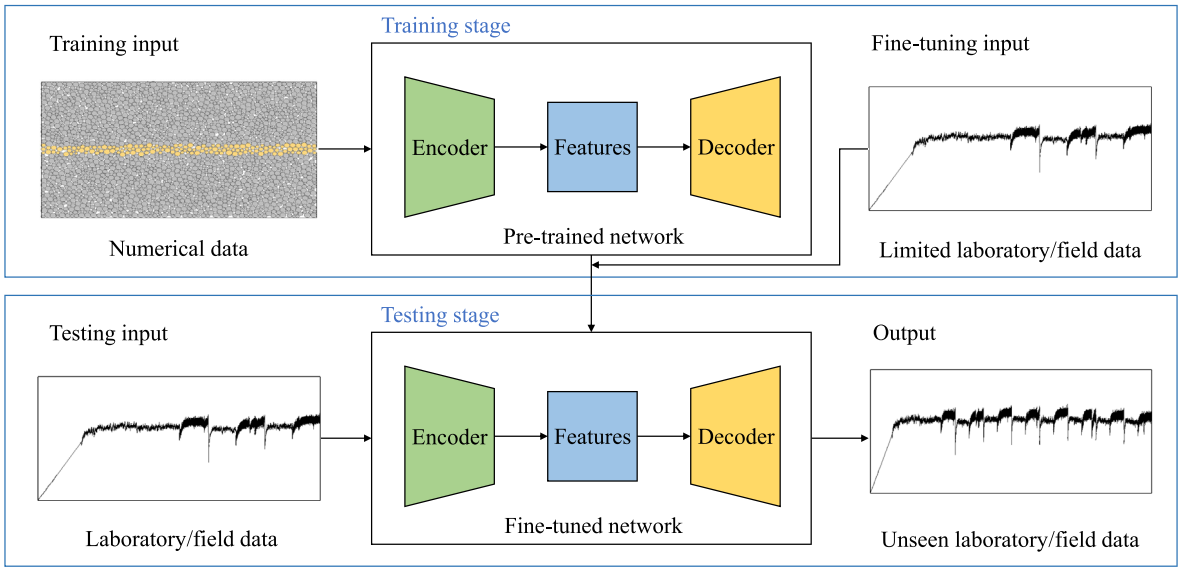

Fig. 10. Schematic diagram of transfer learning analysis using limited laboratory/field data with produced numerical data for data mining.

the assistance of multidisciplinary approaches, such as data analytics and machine learning.

Declaration of competing interest

The authors declare that they have no known competing financial interests or personal relationships that could have appeared to influence the work reported in this paper.

Acknowledgements

This research is supported by National Research Foundation, Singapore under its Intra-CREATE Thematic Grant (Award No. NRF2019-THE001-0002).

References

[1] W.L. Ellsworth, D. Giardini, J. Townend, S. Ge, T. Shimamoto, Triggering of the Pohang, Korea, earthquake (Mw 5.5) by enhanced geothermal system stimulation, Seismol Res. Lett. 90 (2019) 1844–1858, https://doi.org/10.1785/0220190102.
[2] S. Wang, G. Jiang, X. Lei, A.J. Barbour, X. Tan, C. Xu, X. Xu, Three Mw≥ 4.7 earthquakes within the Changning (China) shale gas field ruptured shallow faults intersecting with hydraulic fracturing wells, J. Geophys. Res. Solid Earth 127 (2022), e2021JB022946, https://doi.org/10.1029/2021JB022946.
[3] F.R. Walsh, M.D. Zoback, Oklahoma's recent earthquakes and saltwater disposal, Sci. Adv. 1 (2015), e1500195, https://doi.org/10.1126/sciadv.1500195.
[4] W.L. Ellsworth, Injection-induced earthquakes, Science 341 (2013), 1225942, https://doi.org/10.1126/science.1225942.
[5] F. Grigoli, S. Cesca, E. Priolo, A.P. Rinaldi, J.F. Clinton, T.A. Stabile, B. Dost, M.G. Fernandez, S. Wiemer, T. Dahm, Current challenges in monitoring, discrimination, and management of induced seismicity related to underground industrial activities: a European perspective, Rev. Geophys. 55 (2017) 310–340, https://doi.org/10.1002/2016RG000542.
[6] D. Elsworth, C.J. Spiers, A.R. Niemeijer, Understanding induced seismicity, Science 354 (2016) 1380–1381, https://doi.org/10.1126/science.aal2584.
[7] K.K. Lee, W.L. Ellsworth, D. Giardini, J. Townend, S. Ge, T. Shimamoto, I.W. Yeo, T.S. Kang, J. Rhie, D.H. Sheen, C. Chang, J.U. Woo, C. Langenbruch, Managing injection-induced seismic risks, Science 364 (2019) 730–732, https://doi.org/10.1126/science.aax1878.
[8] H. Hofmann, G. Zimmermann, M. Farkas, E. Huenges, A. Zang, M. Leonhardt, G. Kwiatek, P. Martinez-Garzon, M. Bohnhoff, K.B. Min, P. Fokker, R. Westaway, F. Bethmann, P. Meier, K.S. Yoon, J.W. Choi, T.J. Lee, K.Y. Kim, First field application of cyclic soft stimulation at the Pohang Enhanced Geothermal System site in Korea, Geophys. J. Int. 217 (2019) 926–949, https://doi.org/10.1093/gji/ggz058.
[9] G. Kwiatek, T. Saarno, T. Ader, F. Bluemle, M. Bohnhoff, M. Chendorain, G. Dresen, P. Heikkinen, I. Kukkonen, P. Leary, M. Leonhardt, P. Malin, P. Martínez-Garzón, K. Passmore, P. Passmore, S. Valenzuela, C. Wollin, Controlling fluid-induced seismicity during a 6.1-km-deep geothermal stimulation in Finland, Sci. Adv. 5 (2019) eaav7224, https://doi.org/10.1126/sciadv.aav7224.
[10] A. Zang, G. Zimmermann, H. Hofmann, O. Stephansson, K.B. Min, K.Y. Kim, How to reduce fluid-injection-induced seismicity, Rock Mech. Rock Eng. 52 (2019) 475–493, https://doi.org/10.1007/s00603-018-1467-4.
[11] T.D. Rathnaweera, W. Wu, Y. Ji, R.P. Gamage, Understanding injection-induced seismicity in enhanced geothermal systems: from the coupled thermo-hydro-mechanical-chemical process to anthropogenic earthquake prediction, Earth Sci. Rev. 205 (2020), 103182, https://doi.org/10.1016/j.earscirev.2020.103182.
[12] T.S. Eyre, D.W. Eaton, D.I. Garagash, M. Zecevic, M. Venieri, R. Weir, D.C. Lawton, The role of aseismic slip in hydraulic fracturing-induced seismicity, Sci. Adv. 5 (2019), eaav7172, https://doi.org/10.1126/sciadv.aav7172.
[13] K.H. Palgunadi, A.A. Gabriel, T. Ulrich, J.Á. López-Comino, P.M. Mai, Dynamic fault interaction during a fluid-injection-induced earthquake: the 2017 Mw 5.5 Pohang event, Bull. Seismol. Soc. Am. 110 (2020) 2328–2349, https://doi.org/10.1785/0120200106.
[14] Y. Guglielmi, F. Cappa, J.P. Avouac, P. Henry, D. Elsworth, Seismicity triggered by fluid injection-induced aseismic slip, Science 348 (2015) 1224–1226, https://doi.org/10.1126/science.aab0476.
[15] Z. Ye, A. Ghassemi, Heterogeneous fracture slip and aseismic-seismic transition in a triaxial injection test, Geophys. Res. Lett. 47 (2020), e2020GL087739, https://doi.org/10.1029/2020GL087739.
[16] L. Wang, G. Kwiatek, E. Rybacki, A. Bonnelye, M. Bohnhoff, G. Dresen, Laboratory study on fluid-induced fault slip behavior: the role of fluid pressurization rate, Geophys. Res. Lett. 47 (2020), e2019GL086627, https://doi.org/10.1029/2019GL086627.
[17] Z. Fang, W. Wu, Laboratory friction-permeability response of rock fractures: a review and new insights, Geomech. Geophys. Geo-Energy Geo-Resour. 8 (2022) 1–16, https://doi.org/10.1007/s40948-021-00316-8.
[18] Y. Ji, W. Wu, Injection-driven fracture instability in granite: mechanism and implications, Tectonophysics 791 (2020), 228572, https://doi.org/10.1016/j.tecto.2020.228572.
[19] L. Wang, G. Kwiatek, E. Rybacki, M. Bohnhoff, G. Dresen, Injection-induced seismic moment release and laboratory fault slip: implications for fluid-induced seismicity, Geophys. Res. Lett. 47 (2020), e2020GL089576, https://doi.org/10.1029/2020GL089576.
[20] S. Barbot, Slow-slip, slow earthquakes, period-two cycles, full and partial ruptures, and deterministic chaos in a single asperity fault, Tectonophysics 768 (2019), 228171, https://doi.org/10.1016/j.tecto.2019.228171.
[21] E. Rabinowicz, The nature of the static and kinetic coefficients of friction, J. Appl. Phys. 22 (1951) 1373–1379, https://doi.org/10.1063/1.1699869.
[22] Y. Ida, Cohesive force across the tip of a longitudinal-shear crack and Griffith's specific surface energy, J. Geophys. Res. 77 (1972) 3796–3805, https://doi.org/10.1029/JB077i020p03796.
[23] D.J. Andrews, Rupture propagation with finite stress in antiplane strain, J. Geophys. Res. 81 (1976) 3575–3582, https://doi.org/10.1029/JB081i020p03575.
[24] D.I. Garagash, L.N. Germanovich, Nucleation and arrest of dynamic slip on a pressurized fault, J. Geophys. Res. Solid Earth 117 (2012), B10310, https://doi.org/10.1029/2012JB009209.
[25] F. Ciardo, A.P. Rinaldi, Impact of injection rate ramp-up on nucleation and arrest of dynamic fault slip, Geomech. Geophys. Geo-Energy Geo-Resour. 8 (2022) 28, https://doi.org/10.1007/s40948-021-00336-4.
[26] J.H. Dieterich, Time-dependent friction and the mechanics of stick-slip, in: Rock Friction and Earthquake Prediction, Birkhäuser, Basel, 1978, pp. 790–806.

[27] C.H. Scholz, J.T. Engelder, The role of asperity indentation and ploughing in rock friction-I: asperity creep and stick-slip, Int. J. Rock Mech. Min. Sci. 13 (1976) 149–154, https://doi.org/10.1016/0148-9062(76)90819-6.

[28] A. Ruina, Slip instability and state variable friction laws, J. Geophys. Res. Solid Earth 88 (1983) 10359–10370, https://doi.org/10.1029/JB088iB12p10359.

[29] C. Marone, Laboratory-derived friction laws and their application to seismic faulting, Annu. Rev. Earth Planet Sci. 26 (1998) 643–696, https://doi.org/10.1146/annurev.earth.26.1.643.

[30] L.L. Lavier, X. Tong, J. Biemiller, The mechanics of creep, slow slip events, and earthquakes in mixed brittle-ductile fault zones, J. Geophys. Res. Solid Earth 126 (2021), e2020JB020325, https://doi.org/10.1029/2020JB020325.

[31] R.A. Harries, Large earthquakes and creeping faults, Rev. Geophys. 55 (2017) 169–198.

[32] J.R. Leeman, D.M. Saffer, M.M. Scuderi, C. Marone, Laboratory observations of slow earthquakes and the spectrum of tectonic fault slip modes, Nat. Commun. 7 (2016), 11104, https://doi.org/10.1038/ncomms11104.

[33] S. Barbot, Modulation of fault strength during the seismic cycle by grain-size evolution around contact junctions, Tectonophysics 765 (2019) 129–145, https://doi.org/10.1016/j.tecto.2019.05.004.

[34] C. Mei, S. Barbot, Y. Jia, W. Wu, Experimental evidence for multiple controls on fault stability and rupture dynamics, Earth Planet Sci. Lett. 577 (2022), 117252, https://doi.org/10.1016/j.epsl.2021.117252.

[35] P. Bhattacharya, R.C. Viesca, Fluid-induced aseismic fault slip outpaces pore-fluid migration, Science 364 (2019) 464–468, https://doi.org/10.1126/science.aaw7354.

[36] A. Sáez, B. Lecampion, P. Bhattacharya, R.C. Viesca, Three-dimensional fluid-driven stable frictional ruptures, J. Mech. Phys. Solid. 160 (2022), 104754, https://doi.org/10.1016/j.jmps.2021.104754.

[37] S.D. Davis, W.D. Pennington, Induced seismic deformation in the Cogdell oil field of west Texas, Bull. Seismol. Soc. Am. 79 (1989) 1477–1495, https://doi.org/10.1785/BSSA0790051477.

[38] C.G. Bufe, The Anderson Reservoir seismic gap-induced aseismicity? Eng. Geol. 10 (1976) 255–262, https://doi.org/10.1016/0013-7952(76)90025-9.

[39] O. Scotti, F.H. Cornet, In situ evidence for fluid-induced aseismic slip events along fault zones, Int. J. Rock Mech. Min. Sci. 31 (1994) 347–358, https://doi.org/10.1016/0148-9062(94)90902-4.

[40] F.H. Cornet, J. Helm, H. Poitrenaud, A. Etchecopar, Seismic and aseismic slips induced by large-scale fluid injections, in: Seismicity Associated with Mines, Reservoirs and Fluid Injections, Birkhäuser, Basel, 1997, pp. 563–583.

[41] T.S. Eyre, M. Zecevic, R.O. Salvage, D.W. Eaton, A long-lived swarm of hydraulic fracturing-induced seismicity provides evidence for aseismic slip, Bull. Seismol. Soc. Am. 110 (2020) 2205–2215, https://doi.org/10.1785/0120200107.

[42] S. Cesca, D. Stich, F. Grigoli, A. Vuan, J.Á. López-Comino, P. Niemz, E. Blanch, T. Dahm, W.L. Ellsworth, Seismicity at the Castor gas reservoir driven by pore pressure diffusion and asperities loading, Nat. Commun. 12 (2021) 4783, https://doi.org/10.1038/s41467-021-24949-1.

[43] T.H. Goebel, S.M. Hosseini, F. Cappa, E. Hauksson, J.P. Ampuero, F. Aminzadeh, J.B. Saleeby, Wastewater disposal and earthquake swarm activity at the southern end of the Central Valley, California, Geophys. Res. Lett. 43 (2016) 1092–1099, https://doi.org/10.1002/2015GL066948.

[44] X. Chen, P.M. Shearer, California foreshock sequences suggest aseismic triggering process, Geophys. Res. Lett. 40 (2013) 2602–2607, https://doi.org/10.1002/grl.50444.

[45] R. Bilham, N. Suszek, S. Pinkney, California creepmeters, Seismol Res. Lett. 75 (2004) 481–492, https://doi.org/10.1785/gssrl.75.4.481.

[46] M. Shirzaei, R. Bürgmann, Time-dependent model of creep on the Hayward fault from joint inversion of 18 years of InSAR and surface creep data, J. Geophys. Res. Solid Earth 118 (2013) 1733–1746, https://doi.org/10.1002/jgrb.50149.

[47] J.J. McGuire, P. Segall, Imaging of aseismic fault slip transients recorded by dense geodetic networks, Geophys. J. Int. 155 (2003) 778–788, https://doi.org/10.1111/j.1365-246X.2003.02022.x.

[48] A. Canitano, M. Mouyen, Y.J. Hsu, A. Linde, S. Sacks, H.M. Lee, Fifteen years of continuous high-resolution borehole strainmeter measurements in eastern Taiwan: an overview and perspectives, GeoHazards 2 (2021) 172–195, https://doi.org/10.3390/geohazards2030010.

[49] V. Karabacak, E. Altunel, Z. Cakir, Monitoring aseismic surface creep along the North Anatolian Fault (Turkey) using ground-based LIDAR, Earth Planet Sci. Lett. 304 (2011) 64–70, https://doi.org/10.1016/j.epsl.2011.01.017.

[50] S. Wei, J.P. Avouac, K.W. Hudnut, A. Donnellan, J.W. Parker, R.W. Graves, D. Helmberger, E. Fielding, Z. Liu, F. Cappa, M. Enevae, The 2012 Brawley swarm triggered by injection-induced aseismic slip, Earth Planet, Sci. Lett. 422 (2015) 115–125, https://doi.org/10.1016/j.epsl.2015.03.054.

[51] F. Cappa, M.M. Scuderi, C. Collettini, Y. Guglielmi, J.P. Avouac, Stabilization of fault slip by fluid injection in the laboratory and in situ, Sci. Adv. 5 (2019), https://doi.org/10.1126/sciadv.aau4065 eaau4065.

[52] F. Cappa, Y. Guglielmi, C. Nussbaum, J. Birkholzer, On the relationship between fault permeability increases, induced stress perturbation, and the growth of aseismic slip during fluid injection, Geophys. Res. Lett. 45 (2018) 11012–11020, https://doi.org/10.1029/2018GL080233.

[53] N. Wynants-Morel, F. Cappa, L. De Barros, J.P. Ampuero, Stress perturbation from aseismic slip drives the seismic front during fluid injection in a permeable fault, J. Geophys. Res. Solid Earth 125 (2020), e2019JB019179, https://doi.org/10.1029/2019JB019179.

[54] S. Larochelle, N. Lapusta, J.P. Ampuero, F. Cappa, Constraining fault friction and stability with fluid-injection field experiments, Geophys. Res. Lett. 48 (2021), e2020GL091188, https://doi.org/10.1029/2020GL091188.

[55] M. Alghannam, R. Juanes, Understanding rate effects in injection-induced earthquakes, Nat. Commun. 11 (2020) 3053, https://doi.org/10.1038/s41467-020-16860-y.

[56] Y. Yang, E.M. Dunham, Effect of porosity and permeability evolution on injection-induced aseismic slip, J. Geophys. Res. Solid Earth 126 (2021), e2020JB021258, https://doi.org/10.1029/2020JB021258.

[57] Y. Fang, D. Elsworth, C. Wang, T. Ishibashi, J.P. Fitts, Frictional stability-permeability relationships for fractures in shales, J. Geophys. Res. Solid Earth 122 (2017) 1760–1776, https://doi.org/10.1002/2016JB013435.

[58] W. Zhu, K.L. Allison, E.M. Dunham, Y. Yang, Fault valving and pore pressure evolution in simulations of earthquake sequences and aseismic slip, Nat. Commun. 11 (2020) 4833, https://doi.org/10.1038/s41467-020-18598-z.

[59] L. De Barros, N. Wynants-Morel, F. Cappa, P. Danré, Migration of fluid-induced seismicity reveals the seismogenic state of faults, J. Geophys. Res. Solid Earth 126 (2021), e2021JB022767, https://doi.org/10.1029/2021JB022767.

[60] S.K.Y. Lui, Y. Huang, R.P. Young, The role of fluid pressure-induced aseismic slip in earthquake cycle modulation, J. Geophys. Res. Solid Earth 126 (2021), e2020JB021196, https://doi.org/10.1029/2020JB021196.

[61] K. Im, J.P. Avouac, E.R. Heimisson, D. Elsworth, Ridgecrest aftershocks at Coso suppressed by thermal destressing, Nature 595 (2021) 70–74, https://doi.org/10.1038/s41586-021-03601-4.

[62] E. Tinti, M.M. Scuderi, L. Scognamiglio, G. Di Stefano, C. Marone, C. Collettini, On the evolution of elastic properties during laboratory stick-slip experiments spanning the transition from slow slip to dynamic rupture, J. Geophys. Res. Solid Earth 121 (2016) 8569–8594, https://doi.org/10.1002/2016JB013545.

[63] R. Bürgmann, The geophysics, geology and mechanics of slow fault slip, Earth Planet Sci. Lett. 495 (2018) 112–134, https://doi.org/10.1016/j.epsl.2018.04.062.

[64] D.R. Shelly, Periodic, chaotic, and doubled earthquake recurrence intervals on the deep San Andreas Fault, Science 328 (2010) 1385–1388, https://doi.org/10.1126/science.1189741.

[65] D.M. Veedu, S. Barbot, The Parkfield tremors reveal slow and fast ruptures on the same asperity, Nature 532 (2016) 361–365, https://doi.org/10.1038/nature17190.

[66] C. Mei, S. Barbot, W. Wu, Period-multiplying cycles at the transition between stick-slip and stable sliding and implications for the Parkfield period-doubling tremors, Geophys. Res. Lett. 48 (2021), e2020GL091807, https://doi.org/10.1029/2020GL091807.

[67] M. Calò, C. Dorbath, M. Frogneux, Injection tests at the EGS reservoir of Soultz-sous-Forêts. Seismic response of the GPK4 stimulations, Geothermics 52 (2014) 50–58, https://doi.org/10.1016/j.geothermics.2013.10.007.

[68] C. Mei, Z. Fang, W. Wu, Slip transition of rock fractures due to chemical corrosion, Eng. Geol. 308 (2022), 106801, https://doi.org/10.1016/j.enggeo.2022.106801.

[69] W. Wu, M. Calò, Z. Fang, Laboratory evidence for slip evolution of granite fractures due to chemical stimulation in geothermal reservoirs, Eng. Geol. 306 (2022), 106773, https://doi.org/10.1016/j.enggeo.2022.106773.

[70] Y. Ji, J.S. Yoon, A. Zang, W. Wu, Mitigation of injection-induced seismicity on undrained faults in granite using cyclic fluid injection: a laboratory study, Int. J. Rock Mech. Min. Sci. 146 (2021), 104881, https://doi.org/10.1016/j.ijrmms.2021.104881.

[71] Y. Fang, D. Elsworth, C. Wang, Y. Jia, Mineralogical controls on frictional strength, stability, and shear permeability evolution of fractures, J. Geophys. Res. Solid Earth 123 (2018) 3549–3563, https://doi.org/10.1029/2017JB015338.

[72] E.C. Yildirim, K. Im, D. Elsworth, The influence of fault reactivation on injection-induced dynamic triggering of permeability evolution, Geophys. J. Int. 223 (2020) 1481–1496, https://doi.org/10.1093/gji/ggaa382.

[73] M.M. Scuderi, C. Collettini, The role of fluid pressure in induced vs. triggered seismicity: insights from rock deformation experiments on carbonates, Sci. Rep. 6 (2016), 24852, https://doi.org/10.1038/srep24852.

[74] M.M. Scuderi, C. Collettini, C. Marone, Frictional stability and earthquake triggering during fluid pressure stimulation of an experimental fault, Earth Planet Sci. Lett. 477 (2017) 84–96, https://doi.org/10.1016/j.epsl.2017.08.009.

[75] C. Noël, F.X. Passelègue, C. Giorgetti, M. Violay, Fault reactivation during fluid pressure oscillations: transition from stable to unstable slip, J. Geophys. Res. Solid Earth 124 (2019) 10940–10953, https://doi.org/10.1029/2019JB018517.

[76] M.L. Blanpied, D.A. Lockner, J.D. Byerlee, Fault stability inferred from granite sliding experiments at hydrothermal conditions, Geophys. Res. Lett. 18 (1991) 609–612, https://doi.org/10.1029/91GL00469.

[77] P. Knoll, The fluid-induced tectonic rock burst of March 13, 1989 in Werra potash mining district of the GDR (first results), Gerl. Beitrage Geophys. 99 (1990) 239–245.

[78] R. Ze'ev, D.A. Lockner, Fault weakening and earthquake instability by power lubrication, Nature 467 (2010) 452–455.

[79] J.H. Norbeck, R.N. Horne, Maximum magnitude of injection-induced earthquakes: a criterion to assess the influence of pressure migration along faults, Tectonophysics 733 (2018) 108–118, https://doi.org/10.1016/j.tecto.2018.01.028.

[80] J.H. Dieterich, K.B. Richards-Dinger, K.A. Kroll, Modeling injection-induced seismicity with the physics-based earthquake simulator RSQSim, Seismol Res. Lett. 86 (2015) 1102–1109, https://doi.org/10.1785/0220150057.

[81] B.B.T. Wassing, J.D. Van Wees, P.A. Fokker, Coupled continuum modeling of fracture reactivation and induced seismicity during enhanced geothermal operations, Geothermics 52 (2014) 153–164, https://doi.org/10.1016/j.geothermics.2014.05.001.
[82] J. Rutqvist, A.P. Rinaldi, F. Cappa, G.J. Moridis, Modeling of fault reactivation and induced seismicity during hydraulic fracturing of shale-gas reservoirs, J. Pet. Sci. Eng. 107 (2013) 31–44, https://doi.org/10.1016/j.petrol.2013.04.023.
[83] K. Im, J.P. Avouac, On the role of thermal stress and fluid pressure in triggering seismic and aseismic faulting at the Brawley Geothermal Field, California, Geothermics 97 (2021), 102238, https://doi.org/10.1016/j.geothermics.2021.102238.
[84] A. Amini, E. Eberhardt, S. Rogers, S. Venables, M. Gaucher, Empirical and numerical investigation into the influence of fluid injection volume and rate on induced seismicity in the Montney Formation, northeastern British Columbia, J. Pet. Sci. Eng. 213 (2022), 110423, https://doi.org/10.1016/j.petrol.2022.110423.
[85] I.W. Yeo, M.R.M. Brown, S. Ge, K.K. Lee, Causal mechanism of injection-induced earthquakes through the Mw 5.5 Pohang earthquake case study, Nat. Commun. 11 (2020) 2614, https://doi.org/10.1038/s41467-020-16408-0.
[86] F. Grigoli, S. Cesca, A.P. Rinaldi, A. Manconi, J.A. Lopez-Comino, J.F. Clinton, R. Westaway, C. Cauzzi, T. Dahm, S. Wiemer, The November 2017 Mw 5.5 Pohang earthquake: a possible case of induced seismicity in South Korea, Science 360 (2018) 1003–1006, https://doi.org/10.1126/science.aat2010.
[87] T. Terakawa, W. Seo, K.H. Kim, J.H. Ree, Three-dimensional pore fluid pressures in source region of 2017 Pohang earthquake inferred from earthquake focal mechanisms, Geophys. Res. Lett. 47 (2020), e2019GL085964, https://doi.org/10.1029/2019GL085964.
[88] K.I. Kim, H. Yoo, S. Park, J. Yim, L. Xie, K.B. Min, J. Rutqvist, Induced and triggered seismicity by immediate stress transfer and delayed fluid migration in a fractured geothermal reservoir at Pohang, South Korea, Int. J. Rock Mech. Min. Sci. 153 (2022), 105098, https://doi.org/10.1016/j.ijrmms.2022.105098.
[89] K.W. Chang, H. Yoon, Mitigating injection-induced seismicity along basement faults by extraction: application to 2016-2018 Pohang earthquakes, J. Geophys. Res. Solid Earth 126 (2021), e2020JB021486, https://doi.org/10.1029/2020JB021486.
[90] S.A. Shapiro, K.H. Kim, J.H. Ree, Magnitude and nucleation time of the 2017 Pohang Earthquake point to its predictable artificial triggering, Nat. Commun. 12 (2021) 6397, https://doi.org/10.1038/s41467-021-26679-w.
[91] N.J. Van der Elst, M.T. Page, D.A. Weiser, T.H. Goebel, S.M. Hosseini, Induced earthquake magnitudes are as large as (statistically) expected, J. Geophys. Res. Solid Earth 121 (2016) 4575–4590, https://doi.org/10.1002/2016JB012818.
[92] A. McGarr, Maximum magnitude earthquakes induced by fluid injection, J. Geophys. Res. Solid Earth 119 (2014) 1008–1019, https://doi.org/10.1002/2013JB010597.
[93] Z. Li, D. Elsworth, C. Wang, Constraining maximum event magnitude during injection-triggered seismicity, Nat. Commun. 12 (2021) 1528, https://doi.org/10.1038/s41467-020-20700-4.
[94] M.D. Zoback, S.M. Gorelick, Earthquake triggering and large-scale geologic storage of carbon dioxide, Proc. Natl. Acad. Sci. USA 109 (2012) 10164–10168, https://doi.org/10.1073/pnas.1202473109.
[95] J. Rutqvist, Determination of hydraulic normal stiffness of fractures in hard rock from well testing, Int. J. Rock Mech. Min. Sci. 32 (1995) 513–523, https://doi.org/10.1016/0148-9062(95)00039-J.
[96] Y. Ji, Z. Fang, W. Wu, Fluid overpressurization of rock fractures: experimental investigation and analytical modeling, Rock Mech. Rock Eng. 54 (2021) 3039–3050, https://doi.org/10.1007/s00603-021-02453-8.
[97] M. Galis, J.P. Ampuero, P.M. Mai, F. Cappa, Induced seismicity provides insight into why earthquake ruptures stop, Sci. Adv. 3 (2017), eaap7528, https://doi.org/10.1126/sciadv.aap7528.
[98] M. Leonhardt, G. Kwiatek, P. Martínez-Garzón, M. Bohnhoff, T. Saarno, P. Heikkinen, G. Dresen, Seismicity during and after stimulation of a 6.1 km deep enhanced geothermal system in Helsinki, Finland, Solid Earth 12 (2021) 581–594, https://doi.org/10.5194/se-12-581-2021.
[99] J.U. Woo, M. Kim, D.H. Sheen, T.S. Kang, J. Rhie, F. Grigoli, W.L. Ellsworth, D. Giardini, An in-depth seismological analysis revealing a causal link between the 2017 Mw 5.5 Pohang earthquake and EGS project, J. Geophys. Res. Solid Earth 124 (2019) 13060–13078, https://doi.org/10.1029/2019JB018368.
[100] J.U. Woo, M. Kim, J. Rhie, T.S. Kang, Aftershock sequence and statistics of the 2017 Mw 5.5 Pohang, South Korea, earthquake: implications of fault heterogeneity and postseismic relaxation, Bull. Seismol. Soc. Am. 110 (2020) 2031–2046, https://doi.org/10.1785/0120200059.
[101] P. Wozniakowska, D.W. Eaton, Machine learning-based analysis of geological susceptibility to induced seismicity in the Montney Formation, Canada, Geophys, Res. Lett. 47 (2020), e2020GL089651, https://doi.org/10.1029/2020GL089651.
[102] S. Pawley, R. Schultz, T. Playter, H. Corlett, T. Shipman, S. Lyster, T. Hauck, The geological susceptibility of induced earthquakes in the Duvernay Play, Geophys. Res. Lett. 45 (2017) 1786–1793, https://doi.org/10.1002/2017GL076100.
[103] B. Wang, H. Kao, R.M.H. Dokht, R. Visser, H. Yu, Delineating the controlling factors of hydraulic fracturing-induced seismicity in the Northern Montney Play, Northeastern British Columbia, Canada, with machine learning, Seismol Res. Lett. 93 (2022) 2439–2450, https://doi.org/10.1785/0220220075.
[104] B.K. Holtzman, A. Paté, J. Paisley, F. Waldhauser, D. Repetto, Machine learning reveals cyclic changes in seismic source spectra in Geysers geothermal field, Sci. Adv. 4 (2018), eaao2929, https://doi.org/10.1126/sciadv.aao292.
[105] K. Wang, C.W. Johnson, K.C. Bennett, P.A. Johnson, Predicting fault slip via transfer learning, Nat. Commun. 12 (2021) 7319, https://doi.org/10.1038/s41467-021-27553-5.
[106] K.J. Bergen, P.A. Johnson, M.V.D. Hoop, G.C. Beroza, Machine learning for data-driven discovery in solid Earth geoscience, Science 363 (2019) 1299, https://doi.org/10.1126/science.aau0323.